SPHR: A Soft Pneumatic Hybrid Robot with extreme shape changing and lifting abilities

Matthew R. Devlin[1*], Myia M. Dickens[2], Charles Xiao[1], and Elliot W. Hawkes[1]

***Abstract*— Many soft robots are capable of significantly changing their shape, an ability that can offer advantages in many applications. For instance, such a robot can flatten its body to fit under small gaps and expand to move over large obstacles. Further, because these shape changes are usually driven by a pressurized fluid, if they act over a large area, they have the potential to apply large forces to the world. However, when these same shape changes are used for the locomotion of an untethered robot, they tend to result in slow forward movement. Here we present a hybrid soft-rigid elongated-sphere robot that decouples shape change from locomotion. Pairing a compliant, inflatable outer skin, which changes volume by 15x to both fit under and roll over obstacles and can lift objects up to 30 kg, with a wheeled internal carriage, we obtain relatively fast locomotion. A new two-sided controllable adhesive between the internal carriage and the skin enables the carriage to climb vertically inside the skin, allowing the robot to climb external obstacles. We present the design of the robot, simple modeling of its behavior, and experimental testing. Our work advances the area of hybrid soft-rigid robotics by demonstrating how leveraging the strengths of both soft and rigid systems can have quantifiable performance benefits.**

I. INTRODUCTION

In scenarios requiring navigation through challenging terrain, soft robots have been proposed as viable solutions [1], [2]. In an uncertain and cluttered environment, soft robots that can change shape to fit under, through, or over obstacles, can potentially perform in previously unreachable environments. Further, a soft body could offer advantages if the robot were to fall or be hit by falling debris.

At the same time, soft robots have the potential to leverage the large forces available through fluidic actuation [3] to pry heavy objects off of a victim or open a passageway. This large force arises from the fact that even at relatively low pressures (tens of kilopascals), significant area in contact with a surface (hundreds of square centimeters) results in a large force (thousands of newtons). This phenomenon is leveraged by pneumatic jacks [4], used commonly in the construction industry. When a pump changes a robot's volume very slowly to lift an object, the system is functionally a highly geared device, where the input power is output as a large force with a small velocity.

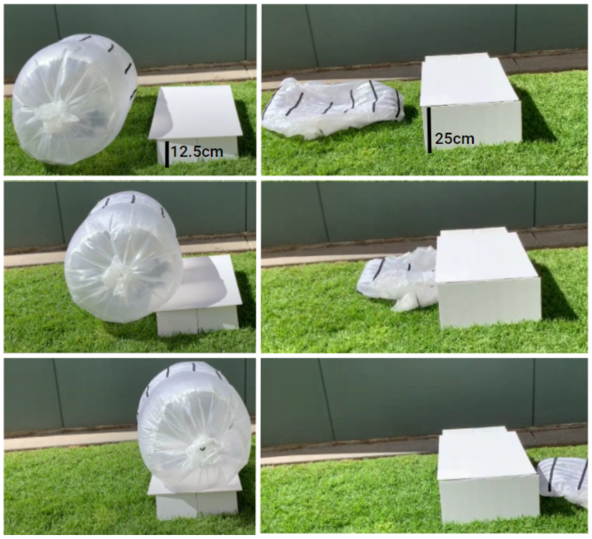

Fig. 1. The soft pneumatic hybrid robot (SPHR). *Left:* The robot is capable of rolling to an obstacle and climbing over it when fully inflated. *Right:* When approaching an obstacle deflated, the robot can pass underneath it.

Accordingly, even as untethered soft robots may have the capacity to produce large forces, they tend to move quite slowly, making their real-world applicability limited. For instance, in [5] the resilient, untethered soft robot's undulating gait resulted in motion at a rate of $0.556\,\mathrm{mm/s^{-1}}$ and self-inflating cellular soft robots moved via peristaltic motion at an even slower rate [3]. In a tethered form, relatively slow rolling was achieved via jamming skin enabled locomotion [6]. Slightly faster is an isoperimetric robot that moves air inside its body with electromagnetic motors rather than pumps, trading off force for speed [7].

In this work, we seek to circumvent this trade off by accomplishing robotic locomotion through traditional wheeled methods, which can result in much faster locomotion than is achieved by a soft robot locomoting via fluidic actuators. We focus specifically on spherical robots, since they offer a rolling morphology and also an enclosed volume which we can use for extreme, fluid-driven shape change and inflation to apply large forces to the world via fluidic actuation. There have been many variants of fixed-shape spherical rolling robots in the literature. Some are driven by moving an internal pendulum or plate that is suspended from a central axis (e.g., [8], [9], [10]). Of these, one proposes a preliminary design of deployment via inflation to achieve a final fixed shape [10]. Others use an internal driving car to shift the center of mass forward to create motion (e.g., [11], [12]).

Here we propose a soft pneumatic hybrid robot (SPHR) that builds upon the previous work in soft robotics and

---

This work was supported in part by NSF Grant 1925373. The work of C. Xiao was supported by the NSF Graduate Research Fellowship Program.

[1] Department of Mechanical Engineering, University of California, Santa Barbara, CA 93106.

[2] Department of Mechanical and Aerospace Engineering, University of California, Irvine, Irvine, CA 92697.

[*] Corresponding author. Email: matthewdevlin@ucsb.edu

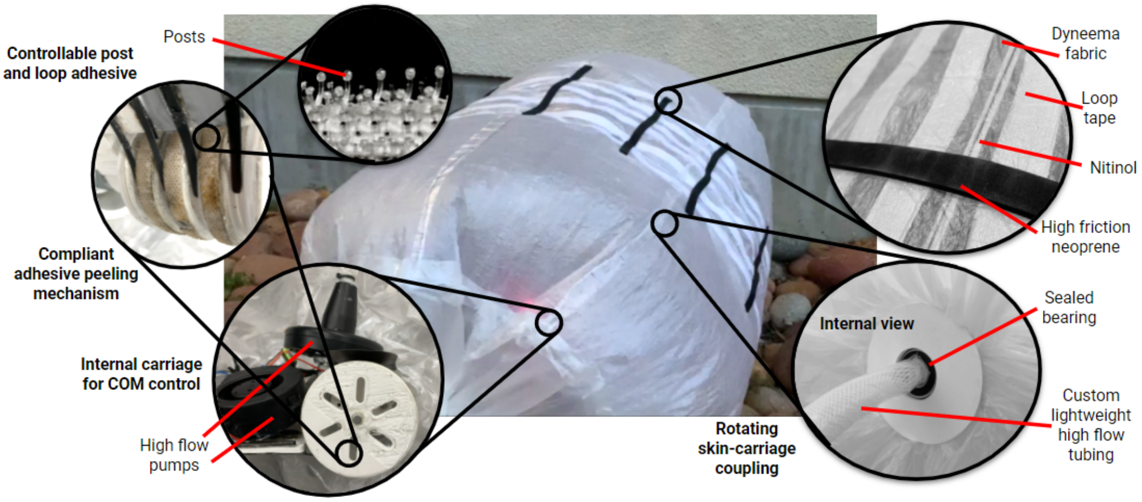

Fig. 2. Overview of the design of the SPHR. At center is the fully inflated, untethered robot. Clockwise from the upper right: the lightweight, strong skin with nitinol ribs that prevent wrinkling when deflated and foam protrusions that add grip; the sealed bearing that allows air to pass into the lightweight woven tubes that are free to rotate with respect to the skin; the internal carriage that controls COM location and carries the pumps; and the custom controllable post-and-loop adhesive, mounted to the wheels and the center track of the skin, providing high shear and adhesion, but peels with minimal force.

spherical robots. The contributions of our work are threefold. First, we present the design of a hybrid robot that combines the abilities of soft robots (extreme shape-change and fluidic-actuation to apply large forces to the environment) with the locomotion speeds of traditional wheeled robots. Second, we develop simple models that describe the behavior of such robots and help inform their design. Third, we introduce a two-sided controllable adhesive that is essential in maximizing the height of obstacles that the SPHR can climb.

The remainder of the paper will be presented in four sections. In Section II, we discuss the design concept of the SPHR, and in Section III, the mathematical analysis of various components required to achieve the desired functionality of the robot. In Section IV, we present an overview of all the components of final design of SPHR, with Section V presenting the validation of each of the chosen components.

II. DESIGN CONCEPT

The key design requirements for the SPHR robot are to: (i) locomote relatively quickly over flat ground without a tether, (ii) pass over obstacles, (iii) pass under obstacles, and (iv) lift heavy objects. To achieve these requirements, our design comprises an internal wheeled carriage, a compliant and airtight skin, a shear-dependent adhesive surface between the carriage and skin, and an inflation system for changing internal volume and pressure. We describe each below.

A. Internal Carriage Design

Locomotion of spherical robots is generally achieved by moving the center of mass (COM) within the robot. Given that our skin changes shape, a rigid axle and pendulum design is not feasible, thus we choose a design with an internal carriage that drives on the inner surface of the skin. In an enclosed system with a circular cross section, climbing is achieved by moving the COM over the edge of the obstacle. In our system, this equates to driving the carriage close to ninety degrees from the default position at the bottom of the circular cross section to the side, cantilevering the COM beyond the edge of the obstacle (see Fig. 1, second photo in climbing sequence). Therefore, the internal carriage must minimize slip with respect to the internal skin in order to climb as high as possible. This slip minimization can be achieved through a wide wheel base for increased surface area and careful material design (see Section II-C).

B. Skin Design

For the skin of our robot, multiple key requirements inform material selection. As mentioned previously, COM control through the internal carriage is critical for this robot, so the skin must be as lightweight as possible. This is because the COM position is a weighted average of the COMs of all the components, and, if the skin were heavy, motion of the internal carriage would not significantly shift the COM. In order to achieve volumetric inflation, it is necessary for the skin to be airtight. Furthermore, to navigate a variety of environments, the skin must be robust against puncture and tearing, while also being strong to resist the stresses involved during lifting operations. Thus a high-strength, tough, lightweight, airtight material is needed. Finally, to allow the internal carriage to smoothly roll inside the skin even when deflated, it must remain unwrinkled along the path of the internal carriage. We design a light, elastic skeleton to meet this requirement, comprising parallel elastic hoops running along the path of the internal carriage (Fig. 2).

C. Controllable Adhesive Design

Controlling the friction and adhesion between the internal carriage and the skin of the robot allows for efficient and effective COM control and locomotion. In order to climb over an obstacle in a skin with a circular cross section, the internal carriage would ideally be able to climb vertically. The material at the interface between the carriage and the skin should have a high shear friction and moderate normal adhesion when loaded in shear to enable climbing (adhesion is required to prevent the internal carriage from pitching backward, as described in Section III). Yet at the same time, the material should have a near-zero normal adhesion for efficient rolling along flat surfaces when not loaded in shear.

This is a very challenging set of requirements that very few materials in the world meet. One is natural gecko adhesive [13], [14], and the bio-inspired controllable adhesives based on the gecko (e.g., [15], [16]). Unfortunately, due to the wrinkling of the skin, not enough contact area is available in our system for synthetic gecko adhesives (less than 80 µm tall) to be a viable option. Therefore, we designed a new controllable adhesive that takes advantage of the fact that we can control the surface structure of contacting surfaces (the wheels and the inside of the skin). The new material is similar to a traditional hook-and-loop fastener such as Velcro®, but instead of hooks, we have designed posts. This design means that as a large shear load is applied, the loops pull on the near-vertical posts, which support the load, yet when a normal load with no shear is applied, the loops simply slide off the posts (see Section III-C). This is substantially different than Velcro®, which requires a large normal load to disengage, even at zero shear. Additionally, our post-and-loop adhesive has much taller (1 mm) features than gecko-inspired adhesives to allow more robust engagement in wrinkled or misaligned scenarios.

D. Inflation System Design

In this robot, a large volume of air (900 L) must be passed across the skin during inflation and deflation to achieve obstacle navigation and lifting. The ideal pump for inflating the robot has a high flow rate while also producing enough pressure to perform lifting tasks. Accordingly, we chose a radial blower for its high flow rate and acceptable pressure, and we added a custom check valve in order to maintain pressures after inflation. For deflation, the same pump could be used with valving to switch its flow direction, however flow losses in commercially available valves are significant. Therefore, we use a simple fan for deflation that is relatively compact and avoids the use of valves. To connect these pumps to the air outside the robot, lightweight tubing must pass from the internal carriage through the skin of the robot. During locomotion, the skin must be able to rotate freely about the tubes without kinking the tubes or limiting the movement of the skin. In our robot, sealed bearings connect the skin to custom, torsionally stiff and lightweight tubing. This tubing has an internal braided polyester sleeve, to increase torsional stiffness that is covered by an airtight polyethylene tube (Fig. 2, inset).

III. MODELING

A. Obstacle Interaction Model

This section describes how movement of the center of mass (COM) within the inflated skin enables the robot to overcome obstacles. We relate the robot COM position to the maximum obstacle height that can be climbed. We note that various previous work has looked at this general problem (e.g., [12], [10]), and our addition is an analysis of interaction forces required for this behavior without slipping.

Assuming a circular cross-section of the inflated skin and a rectangular cross-section of the obstacle (free-body diagram in Fig. 3), we can write the static balance equations (summing moments about the center of the circle) as:

$$\sum F_x = 0 = f_g - N_O \sin(\theta_O) + f_O \cos(\theta_O) \tag{1}$$

$$\sum F_y = 0 = N_g - (M+m)g + N_O \cos(\theta_O) + f_O \sin(\theta_O) \tag{2}$$

$$\sum M_z = 0 = R(f_g + f_O) - (M+m)g r_{cm} \sin(\theta) \tag{3}$$

where N_O is the normal force applied to the robot from the obstacle, θ_O is the angle that the obstacle makes contact with the skin with respect to vertical, f_O is the frictional force between the skin and the obstacle, N_g is the normal force applied on the robot from the ground, M is the mass of the skin of the robot, m is the mass of the internal carriage, R is the radius of the skin of the robot, and h is the height of the obstacle.

While this model is statically indeterminate in general, if we look specifically at the case where the robot is about to roll over the obstacle, N_g and f_g go to zero, and we can solve for the maximum climbable obstacle height, h_{max}, as:

$$h_{max} = R - R\cos\left(\sin^{-1}\left(\frac{r_{cm}\sin(\theta)}{R}\right)\right), \tag{4}$$

where R is the radius of the inflated skin, r_{cm} is the radius to the COM, and θ is the maximum angle from the vertical that the COM of the robot can achieve before slipping. We can also solve for the required frictional force, f_O, between the skin and the obstacle as:

$$f_O = (M+m)g\sqrt{1-\left(\frac{R-h}{R}\right)^2} \tag{5}$$

where f_O is the frictional force between the skin and the obstacle, M is the mass of the skin of the robot, m is the mass of the internal carriage, R is the radius of the skin of the robot, and h is the height of the obstacle.

We gain two insights from these relationships. First, the climbable obstacle height, h_{max}, is maximized when the radius to the COM approaches the skin radius. Second, the required friction force between the skin and the obstacle grows with increasing h. One option to provide a large enough force is to incorporate protrusions on the outside of the skin, which locally change the contact angle, allowing a relatively low coefficient of friction to provide a relatively high friction force before slipping.

B. Internal Static Analysis

Knowing how the position of the robot COM inside the skin relates to the height of obstacle that can be climbed, in this section we describe how the shape and mass distribution

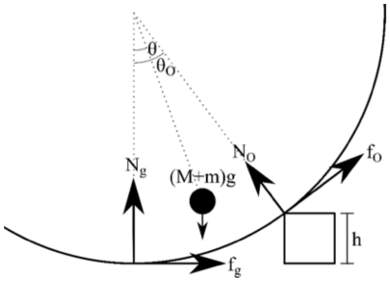

Fig. 3. Geometry and variables used for obstacle interaction model.

of internal carriage, as well as its interaction forces with the skin, affect the achievable COM position.

We again set up the static balance equations based on the geometry shown in Fig. 4, assuming a fixed skin, and write

$$\sum F_x = 0 = -N_1 \sin(\theta - \gamma_1) \\ -N_2 \sin(\theta + \gamma 2) + f \cos(\theta + \gamma 2) \tag{6}$$

$$\sum F_y = 0 = N - mg + N_1 \cos(\theta - \gamma 1) \\ +N_2 \cos(\theta + \gamma_2) + f \sin(\theta + \gamma 2) \tag{7}$$

$$\sum M_z = 0 = -r_m mg \sin(\theta) + R_f \tag{8}$$

where N_1 is the normal force exerted on the smaller coaster wheel of the internal carriage, N_2 is the normal force exerted on the larger driving wheel of the internal carriage, θ is the angle between the vertical and the carriage COM, γ_1 is the angular position of the smaller wheel with respect to the carriage COM, γ_2 is the angular position of the larger wheel with respect to the carriage COM, m is the mass of the internal carriage, f is the shear force the skin applies to the larger wheel, and r_m is the radius to the COM of the internal carriage, and R is the radius of the skin. Solving these equations for the normal and shear forces required for the internal carriage to climb a certain angle θ along the internal surface of the skin, N, previously N_2, and f_s respectively, yields:

$$N_2 = mg \frac{r_m \sin(\theta) \cos(\gamma_1 + \gamma 2) - R \sin(\theta - \gamma 1)}{R \sin(\gamma_1 + \gamma_1)} \tag{9}$$

$$f_s = \frac{mgr_m \sin(\theta)}{R} \tag{10}$$

Using Eq. 9 and 10, we can plot the required normal and shear forces necessary to climb a given angle (Fig. 5). This model reflects the influence of internal carriage design parameters. The height of the COM on the internal carriage should be as close to the internal skin as possible. This can be achieved through decreasing the wheel size of the robot, or by decreasing the length of the internal carriage. It should be noted that for larger climb angles, adhesion, shown through a negative normal force, is required in order to reach beyond 70 degrees.

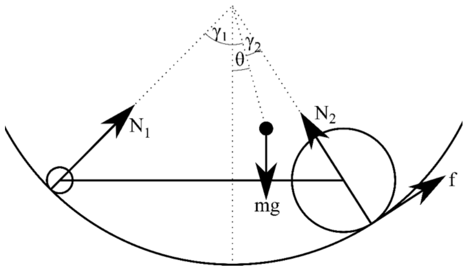

Fig. 4. Geometry and variables used for internal static analysis.

C. Post-and-loop Material

To better understand the trends of the behavior of the controllable adhesive material, we present a simple model. The model relates the geometric structure of the two sides of the material (posts and loops) to the limit curve in force space (a curve that defines the maximum force that can be resisted in any direction).

We start with the assumption that the posts are vertical and have a small spherical cap (Fig. 6). For a loop that is around a post, we seek to determine the largest load angle, θ_{pull}, measured from the horizontal, that a force, F_{pull}, can be applied. Given a coefficient of friction between the post-and-loop, μ_{p-l}, and the tangent angle of the spherical cap where it intersects the post, θ_{cap}, measured from the vertical, we can write

$$\theta_{pull} = \theta_{cap} + \arctan(\mu_{p-l}). \tag{11}$$

This maximum load angle assumes no bending of the post. However, as the shear load becomes larger and larger, the post will deform more, decreasing the maximum load angle until it should reach zero at a large enough shear force. Thus qualitatively, we expect a limit curve that shows zero adhesion (negative normal force) for all load angles greater than θ_{pull} and a decreasing maximum load angle with increasing shear. Interestingly, this is the same qualitative behavior found in synthetic controllable gecko adhesives [16], [15].

IV. FABRICATION

Our modeling suggests that obstacle climbing is maximized when the COM is as close to surface as possible. To build a physical robot, this translates to a lightweight skin with a much heavier internal carriage. For this reason, the skin of the SPHR was constructed from 0.34oz Dyneema, which is a lightweight, durable, and ripstop fabric. Before rolling a rectangle (172 cmx55 cm) of Dyneema into an elongated-sphere, two hemispheres connected by a cylinder, to form the skin of the SPHR, the loop component of hook-and-loop tape is applied in strips along what will be the driving axis of the robot. The loop strips are spaced such that the wheels of the internal carriage will be in constant contact with them along the width of the driving axis. Additionally, two pieces of 0.75 mm nitinol backed with loop tape are placed to decrease wrinkling along the driving axis. On the opposite side of this Dyneema rectangle, strips of 3 mm

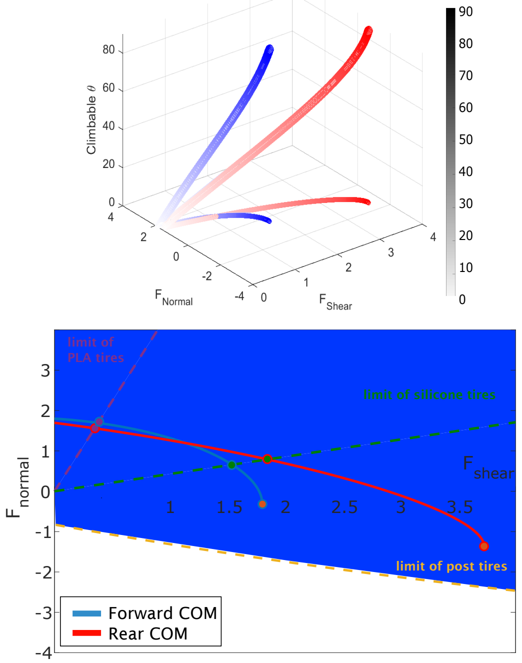

Fig. 5. *Top:* A three-dimensional representation of the climbable angles, θ, as a function of shear and normal forces acting on the front wheels of the internal carriage. Each climbable angle requires a unique combination of shear and normal force. The blue and red curves represent a COM closer to the front and rear wheels respectively An orthogonal projection to the 3D curve is shown on the x-y plane. *Bottom:* The same red and blue curves are shown in the x-y plane, now with an overlay of the limits of shear and normal force available with different material tires. The dotted lines represent different tire materials, with a slope corresponding to their respective coefficient of friction. Dots represent the point of highest predicted climbing for each COM location and tire material. For the post-and-loop tires, even at 90° (the end of the red and blue curves), the limit is not reached. In Fig. 8 these forces are mapped to the corresponding climbing angle θ.

adhesive-backed neoprene are placed perpendicular to the driving axis to provide regions of increased surface friction to benefit obstacle climbing. To finish the skin of this robot, the flat rectangle is taped end-to-end into an elongated-sphere. The internal carriage is placed within the skin, with the volume control tubing and bearing assemblies simply zip-tied to loose ends of the SPHR skin. After full assembly, the SPHR skin weighs approximately 250 g.

The internal carriage assembly consists of two driving wheels at the front with a passive wheel in the back. Two 3D printed wheels with strips of the posts, described in Section III-C, separated by grooves (Fig. 2) allow for vertical climbing. Therefore, motor selection for the carriage is dependent on the mass of the robot so that the motors provide sufficient torque to drive the robot vertically against its own weight. 12V 120rpm Geartisan motors were used in this carriage, powered by 18650 Lithium-ion batteries. After driving the post covered wheels over the loop tape, the loop tape is disconnected by compliant fiberboard fingers that run along the grooves of the carriage wheels. To communicate wirelessly with the internal carriage, a FlySky FS-iA6B receiver is used along with a FlySky FS-iX transmitter. The pumps onboard the internal carriage are high flow rate radial blowers. For inflation, a 12V 50W MorTime air pump is used alongside a 12V, 5W flatpack radial blower for deflation. For high flow rate deflation across a low pressure differential, it is beneficial to have a low pressure, active pump rather than relying on valving which is often bulky for the flow rates needed. After all assembled, the internal carriage weighs approximately 1100 g.

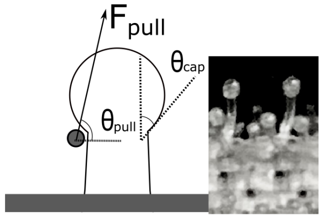

Fig. 6. *Left:* Geometric parameters for the hook-and-post model. *Right:* Image of two individual posts, showing the nearly spherical cap (post height is 1 mm).

To enable pumping air in and out of the skin, sealed bearing assemblies are attached to the sides of the Dyneema tube. To connect the pumps on the internal carriage to the skin of the SPHR, custom, low mass tubing was constructed by adhering LDPE flat tubing to the compressed section of electrical sleeving. This created a torsionally stiff, high flow rate, and low mass solution. Compared to conventional pneumatic tubing of the same diameter, this custom braid-reinforced tubing is 10x lighter, allowing for greater COM control for obstacle climbing.

V. EXPERIMENTAL RESULTS

In this section, we report the results of a series of tests designed to verify the modeling and to characterize and demonstrate the performance of the robot.

A. *Obstacle Interaction Model Verification*

The height of an obstacle that the robot can climb depends on the horizontal and vertical position of the COM within the robot, as modeled in Section III-A and Eq. 4. To validate this model, we constructed three sets of simple non-elongated spheres, with each set having a different diameter. Each set contained three spheres with the same diameter, but with a different location of the COM. The COM location was calculated via a weighted average of components, then verified by using a force gauge placed tangent to the sphere, opposite of the off-center COM. The tangent force required to prevent the sphere from rolling on flat ground was measured, and COM position verified, using a static moment balance across the geometric center of the sphere. Then, each sphere was placed in contact with a rectangular prism with a known height. The COM of the sphere was oriented at 90° from the vertical, in the direction of the obstacle. The sphere was then released, and a success was recorded if the sphere rolled onto the obstacle. If the sphere could successfully climb the obstacle, the obstacle height was incremented by approximately a centimeter. This was repeated until an obstacle height at which the sphere could not successfully climb for all five trials was reached.

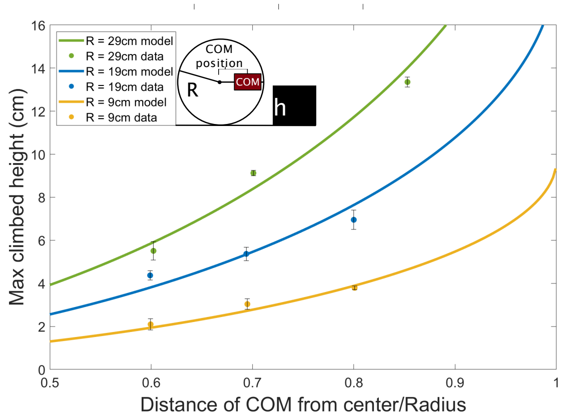

Fig. 7. Results of testing to verify the obstacle interaction model, shown in (4). The maximum height of a climbable obstacle is plotted as a function of the COM placement (measured as a distance from the center and normalized by the radius). The model is shown as curves, and the data as points (average and one standard deviation).

B. *Internal Statics Model Verification*

At the same time, the reachable positions of the COM inside the robot depend on the mass distribution of the internal carriage and its achievable interaction forces with the inside of the skin, as modeled in Section III-B and shown in Fig. 5. To validate this model, an internal carriage with known dimensions and a variable COM location was driven up a constant-curvature ramp, representing the inside of the inflated skin, until it slipped. Climb angles were measured optically and processed with ImageJ. We varied two parameters: the interacting materials (on the tire and ramp), and the COM placement on the car. The three material combinations were: PLA tires on Dyneema skin, Dragonskin 10 silicone rubber tires on Dyneema skin, and custom post tires on custom loop skin (the two components of the post-and-loop adhesive. The two COM placements were forward and rearward. Angles were tested up to 90°. Results are shown in Fig. 8, overlayed with the predictions from (9) and (10). The curves are plotted as functions of the arc length of the normal-shear curve, such that a single axis could be used. We note that the points for the post-and-loop combination did not slip, but rather held to maximum angle tested.

C. *Post-and-loop Material Characterization*

To characterize the adhesion of the post-and-loop material, a load was applied to a 1.5 cm^2 sample of the post material affixed to a sample of the looped counterpart. A small pre-load of approximately 0.2 N was applied to engage the material, and the post material sample was pulled in angles ranging from pure normal to pure shear until failure using a Mark-10 M3-5 force gauge. To evaluate the friction of the sample, a positive normal force was applied in varying angles until the post sample slipped on the loop material. The maximum compressive force was recorded and separated in the corresponding normal and shear components. The findings of this experiment are plotted in Fig. 9. As predicted by our qualitative modeling in Section III-C, we see zero adhesive force when the load is in the negative normal direction, and a decreasing loading angle at high levels of shear. The zero adhesive force for negative normal forces is a critical trait that allows for easy rolling of the wheels of the internal carriage. Standard hook-and-loop material has a high level of adhesion when pulled in the normal direction, meaning significant torque and energy would be required for the robot to move.

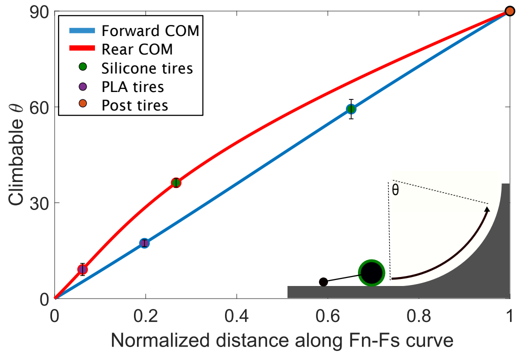

Fig. 8. Model, presented in (9) and (10), and data relating the tire material and internal carriage COM location to the maximum climbable angle of a curved surface (representing the inside of the inflated robot skin). The x-axis represents the distance along the curve in force space, normalized by its length. While PLA and silicone tires slipped at certain angles, the post-and-loop tires did not slip at the maximum angle tested (90°).

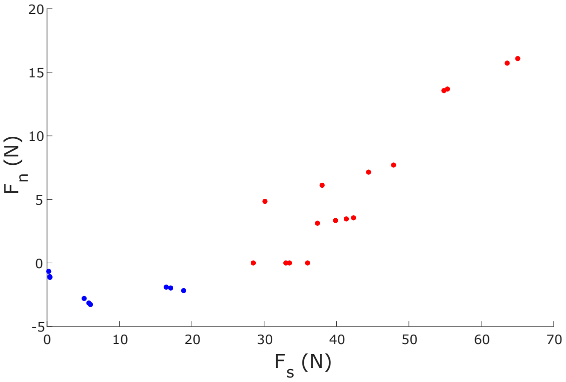

Fig. 9. Limit curve of our post-and-loop controllable adhesive.

D. *Robot Performance*

1) Robot Volume Control Characterization: To evaluate the volume control of this robot, a series of inflation and deflation cycles were run over the lifespan of the battery of the robot. On a single charge, the robot was able to inflate and deflate 15 times. Evaluated in ImageJ, the maximum robot volume was calculated as a cylinder evolving across multiple timepoints. The maximum inflated cylindrical dimensions of this robot were a diameter of 55 cm and a length of 62 cm resulting in a maximum volume of 147 L. The minimum volume was approximated as a cone with the same diameter

Fig. 10. *Left:* From top to bottom, an inflated SPHR navigates smoothly across loose rocks. *Middle:* Reaching an obstacle, the robot is able to inflate and climb an obstacle 12 cm in height. *Right:* After driving deflated to crawl under an obstacle, the robot is able to inflate and lift the object.

of the inflated cylinder mentioned above, using the same height as the robot of 12 cm, resulting in a minimum volume of 9.5 L. This is a total volume change of approximately 15x.

2) Robot Locomotion Robustness: To test robustness, the SPHR was driven over multiple surfaces including grass, pavement, and loose stones (with diameters of approximately 5 cm), as shown in Fig. 10, *left*. On grass and pavement, the robot was able to smoothly navigate without needing to inflate, however, on the loose stones, the inflation of the skin enabled the robot to traverse the mixed terrain. In both cases, the top speed of the robot was greater than $180\,\mathrm{mm\,s^{-1}}$.

Next we tested the ability for the SPHR to climb over and squeeze under obstacles. The robot is able to climb over obstacles that are 12.5 cm tall when fully inflated (Fig. 10, *middle*). When deflated, the robot can squeeze under obstacles 12 cm high.

3) Lifting Capacity: The deflated SPHR is able to drive under an obstacle with 12 cm of clearance, the height of the deflated robot. Through inflating over its large surface area, the robot is able to easily lift a 31 kg table (Fig. 10, *right*). With an inflated footprint of $0.3\,\mathrm{m}^2$, and rated pump pressure of 2.8 kPa, the robot is capable of lifting a theoretical 100 kg.

VI. CONCLUSIONS AND FUTURE WORK

This work reports a proof-of-concept robot that is capable of untethered locomotion, obstacle climbing, extreme shape change, and volumetric actuation. The SPHR leverages the advantages of traditional wheeled robotics for locomotion speed, and the strengths of soft robotics for its shape changing and high-force capabilities. We have demonstrated the benefits of a soft-rigid hybrid robot to demonstrate extreme shape change and lifting ability without sacrificing the locomotion speeds of tradition wheeled robots. Using simple models, we describe the behavior of our robot and develop an understanding of the optimizable parameters of our system. In order to maximize obstacle climbing, we created a controllable adhesive to enable vertical climbing of our internal carriage.

In the future, we will further characterize the controllable adhesive, as well as optimize the design of the robot. Several parameters can be altered depending on the application; for instance, a higher pressure pump for lifting operations, or a larger radius skin for larger obstacle navigation. We also envision developing stand-alone skins with integrated inflation devices that can be rapidly deployed to various current wheeled robotic systems (in a manner analogous to other robotic skins [17]).

REFERENCES

[1] S. Kim, C. Laschi, and B. Trimmer, "Soft robotics: a bioinspired evolution in robotics," *Trends in biotechnology*, vol. 31, no. 5, pp. 287–294, 2013.

[2] D. Rus and M. T. Tolley, "Design, fabrication and control of soft robots," *Nature*, vol. 521, no. 7553, pp. 467–475, 2015.

[3] M. R. Devlin, B. T. Young, N. D. Naclerio, D. A. Haggerty, and E. W. Hawkes, "An untethered soft cellular robot with variable volume, friction, and unit-to-unit cohesion," *IEEE International Conference on Intelligent Robots and Systems*, pp. 3333–3339, oct 2020.

[4] J.-C. Maré, O. Geider, and S. Colin, "An improved dynamic model of pneumatic actuators," *International Journal of Fluid Power*, vol. 1, no. 2, pp. 39–49, 2000.

[5] T. T., S. F., MosadeghBobak, G. C., WehnerMichael, Karpelson-Michael, W. J., and W. M., "A Resilient, Untethered Soft Robot," *Soft Robotics*, vol. 1, no. 3, pp. 213–223, sep 2014.

[6] E. Steltz, A. Mozeika, N. Rodenberg, E. Brown, and H. M. Jaeger, "Jsel: Jamming skin enabled locomotion," in *2009 IEEE/RSJ International Conference on Intelligent Robots and Systems*. IEEE, 2009, pp. 5672–5677.

[7] N. S. Usevitch, Z. M. Hammond, M. Schwager, A. M. Okamura, E. W. Hawkes, and S. Follmer, "An untethered isoperimetric soft robot," *Science Robotics*, vol. 5, no. 40, 2020.

[8] S. Asiri, F. Khademianzadeh, A. Monadjemi, and P. Moallem, "The design and development of a dynamic model of a low-power consumption, two-pendulum spherical robot," *IEEE/ASME Transactions on Mechatronics*, vol. 24, no. 5, pp. 2406–2415, 2019.

[9] R. Mukherjee, M. A. Minor, and J. T. Pukrushpan, "Motion planning for a spherical mobile robot: Revisiting the classical ball-plate problem," *J. Dyn. Sys., Meas., Control*, vol. 124, no. 4, pp. 502–511, 2002.

[10] F. C. Bruhn, H. Kratz, J. Warell, C.-I. Lagerkvist, V. Kaznov, J. A. Jones, and L. Stenmark, "A preliminary design for a spherical inflatable microrover for planetary exploration," *Acta Astronomica*, vol. 63, no. 5, pp. 618–631.

[11] A. Bicchi, A. Balluchi, D. Prattichizzo, and A. Gorelli, "Introducing the" sphericle": an experimental testbed for research and teaching in nonholonomy," in *Proceedings of International Conference on Robotics and Automation*, vol. 3. IEEE, 1997, pp. 2620–2625.

[12] Q. Zhan, Y. Cai, and C. Yan, "Design, analysis and experiments of an omni-directional spherical robot," in *2011 IEEE International Conference on Robotics and Automation*. IEEE, 2011, pp. 4921–4926.

[13] K. Autumn, Y. A. Liang, S. T. Hsieh, W. Zesch, W. P. Chan, T. W. Kenny, R. Fearing, and R. J. Full, "Adhesive force of a single gecko foot-hair," *Nature*, vol. 405, no. 6787, pp. 681–685, 2000.

[14] K. Autumn, M. Sitti, Y. A. Liang, A. M. Peattie, W. R. Hansen, S. Sponberg, T. W. Kenny, R. Fearing, J. N. Israelachvili, and R. J. Full, "Evidence for van der waals adhesion in gecko setae," *Proceedings of the National Academy of Sciences*, vol. 99, no. 19, pp. 12 252–12 256, 2002.

[15] A. Parness, D. Soto, N. Esparza, N. Gravish, M. Wilkinson, K. Autumn, and M. Cutkosky, "A microfabricated wedge-shaped adhesive array displaying gecko-like dynamic adhesion, directionality and long lifetime," *Journal of the Royal Society Interface*, vol. 6, no. 41, pp. 1223–1232, 2009.

[16] P. Day, E. V. Eason, N. Esparza, D. Christensen, and M. Cutkosky, "Microwedge machining for the manufacture of directional dry adhesives," *Journal of Micro and Nano-Manufacturing*, 2013.

[17] J. W. Booth, D. Shah, J. C. Case, E. L. White, M. C. Yuen, O. Cyr-Choiniere, and R. Kramer-Bottiglio, "Omniskins: Robotic skins that turn inanimate objects into multifunctional robots," *Science Robotics*, vol. 3, no. 22, 2018.